

Technical Paper

Int'l J. of Aeronautical & Space Sci. 13(3), 296–305 (2012)
DOI:10.5139/IJASS.2012.13.3.154



Effects of Angles of Attack and Throttling Conditions on Supersonic Inlet Buzz

Hyuck-Joon Namkoug*

Department of Aerospace Engineering, Seoul National University, Seoul 151-744, Korea

Wooram Hong**

Interdisciplinary Program in Computational Science & Technology, Seoul National University, Seoul 151-742, Korea

Jung-Min Kim***

Department of Aerospace Engineering, Seoul National University, Seoul 151-744, Korea

JunSok Yi****

Department of Aerospace Engineering, Seoul National University, Flight Vehicle Research Center (FVRC), Seoul 151-744, Korea

Chongam Kim*****

Institute of Advanced Aerospace Technology, Department of Aerospace Engineering, Seoul National University, Seoul 151-744, Korea

Abstract

A series of numerical simulations are carried out to analyze a supersonic inlet buzz, which is an unsteady pressure oscillation phenomenon around a supersonic inlet. A simple but efficient geometry, experimentally adopted by Nagashima, is chosen for the analysis of unsteady flow physics. Among the two sets of simulations considered in this study, the effects of various throttling conditions are firstly examined. It is seen that the major physical characteristic of the inlet buzz can be obtained by inviscid computations only and the computed flow patterns inside and around the inlet are qualitatively consistent with the experimental observations. The dominant frequency of the inlet buzz increases as throttle area decreases, and the computed frequency is approximately 60Hz or 15% lower than the experimental data, but interestingly, this gap is constant for all the test cases and shock structures are similar. Secondly, inviscid calculations are performed to examine the effect regarding angle of attack. It is found that patterns of pressure oscillation histories and distortion due to asymmetric (or three-dimensional) shock structures are substantially affected by angle of attack. The dominant frequency of the inlet buzz, however, does not change noticeably even in regards to a wide range of angle of attacks.

Key words: supersonic inlet buzz, effect of angle of attack, asymmetric shock structure, distortion

This is an Open Access article distributed under the terms of the Creative Commons Attribution Non-Commercial License (<http://creativecommons.org/licenses/by-nc/3.0/>) which permits unrestricted non-commercial use, distribution, and reproduction in any medium, provided the original work is properly cited.



* Ph. D. Student
** Ph. D. Student
*** M. S. Student
**** Ph. D. Student
***** Professor, Corresponding author: chongam@snu.ac.kr

1. Introduction

The supersonic inlet of the air-breathing engine under operating conditions is exposed to various throttle and angle of attack conditions. In these conditions, it is required to keep a certain quantity of mass flow rate for stable combustion. Compression and deceleration of the incoming flow to a proper Mach number should be achieved without any compressors. Around the supersonic inlet, the shockwave structure is developed by an external inflow condition and internal back pressure from the combustion chamber. This shockwave structure determines the physical properties of the captured air. The supersonic inlet is geometrically simple and its components are just a couple of parts, which are center-body and cowl. Despite the inlets simplicity, complex physical phenomena usually occur inside the engine. Especially, as angle of attack increases, it becomes more asymmetric and complicated.

Shockwave-shockwave interactions (SWI) and shockwave-boundary layer interactions (SWBLI) are typical phenomena of the supersonic inlet and these interactions induce self-excited shock oscillations, which lead to high amplitude variations of the inlet mass flow rate and pressure. Inconsistent mass flow rate incurs severe unsteadiness because the combustion process itself fluctuates heavily. This sequence of unsteady processes is referred to as inlet buzz, which provokes a number of efficiency problems regarding the ramjet. The inlet buzz can cause more serious problems such as thrust loss, non-starting of the engine, and even structural damages to the aircraft [1, 2]. In order to define the buzz occurrence mechanism and to control it, many precedent researches have been conducted in experimental and/or numerical analysis fields. The inlet buzz was first observed and described by Oswatitsch[3]. Later, Dailey [4] found that a SWBLI causes a flow separation on the compression surface, and this separation arises to an inlet buzz (Dailey type buzz). Ferri *et al.* [5] found that a SWI also generates an inlet buzz (Ferri type buzz) by creating a shear layer. Ngashima *et al.* [6] conducted an inlet buzz experiment by controlling the throttling ratio. Based on these earlier experimental studies, some numerical simulations have been carried out to explain the onset mechanism of the inlet buzz. Newsome [7] simulated an inlet buzz with Nagashima's geometry and Lu and Jian [8] adopted Dailey's geometry. Trapier *et al.* [9] captured both the Ferri type and Dailey type buzzes through both experimental and numerical studies.

Today's supersonic air-breathing engine is required to perform well at high angles of attack during tactical operations. However, axisymmetric inlet performance deteriorates rapidly as the angle of attack increases, as

unfavorable factors for combustion such as asymmetric shock structures and non-uniform pressure distribution are generated. It is known that a serious subsonic diffuser flow separation problem, one of the unfavorable factors for combustion, occurs at a high angle of attack. This results in poor combustor performance and eventually the combustor blows out due to this separation [10]. Therefore, to predict engine performance at a non-zero angle of attack, both internal flow characteristics and shock structures should be monitored. Precedent researchers investigated the effects of internal flow characteristics to engine performance at a moderate angle ($0^\circ \sim 9^\circ$) of attack. Nevertheless, there are few investigations of axisymmetric inlet buzz under the attack angled flow condition [6, 11, 12]. Common results of these investigations are that the shock structure becomes more asymmetric as attack angle increases but buzz frequency is almost constant. To predict engine performance during inlet buzz at increased attack angles, it requires more studies that focus on asymmetric internal flow physics such as slip line and distortion.

In this research, the axisymmetric inlet buzz is simulated under various throttle and angle of attack conditions. Inviscid simulations are conducted at zero angle of attack and validated with experiment [6] and turbulent flow simulation data [13]. These validation works show that both inviscid and turbulent flow simulations have similar tendency in that the dominant buzz frequency reduces with the increased throttle area in spite of different local flow physics and values of some variables. In the next step, the effects of different attack angles, from 0° to 10° , are analyzed by inviscid flow calculations. From these results, flow characteristics such as dominant frequency, asymmetric shock structure and distortion are examined with the main interest of inviscid primary flow physics.

2. Numerical Method

2.1 Governing Equation

Inlet buzz is a strong unsteady phenomena accompanying high frequency pressure oscillation, so buzz simulation requires expensive computational cost, i.e. time and resources. To reduce computational cost while maintaining analysis level of qualitative effect from angle of attack of the inlet body, inviscid flow simulations were conducted. For the inviscid simulation, three-dimensional Euler equations are adopted. The Euler equations are expressed as follows:

$$\frac{\partial Q}{\partial t} + \frac{\partial E}{\partial x} + \frac{\partial F}{\partial y} + \frac{\partial G}{\partial z} = 0,$$

$$Q = \begin{bmatrix} \rho \\ \rho U \\ \rho V \\ \rho W \\ E_t \end{bmatrix}, \quad E = \begin{bmatrix} \rho U \\ \rho U^2 + P \\ \rho UV \\ \rho UW \\ (E_t + P)U \end{bmatrix}, \quad F = \begin{bmatrix} \rho V \\ \rho UV \\ \rho V^2 + P \\ \rho VW \\ (E_t + P)V \end{bmatrix}, \quad G = \begin{bmatrix} \rho W \\ \rho UW \\ \rho VW \\ \rho W^2 + P \\ (E_t + P)W \end{bmatrix} \quad (1)$$

As a spatial flux scheme, AUSMPW+[14] is used to remove oscillations of AUSM+ near wall where a strong shock passes by, while maintaining the accuracy of the original scheme. A second-order MUSCL[15] and LU-SGS[16](Lower-Upper Symmetric Gauss-Seidel) time integration method is adopted in this solver, and a dual time stepping method is employed for an unsteady simulation.

2.2 Grid System and Boundary Condition

An axisymmetric engine configuration [6] is used in the current study. As shown in Fig. 1-(a), the engine has a center-body, cowl, and plug components.

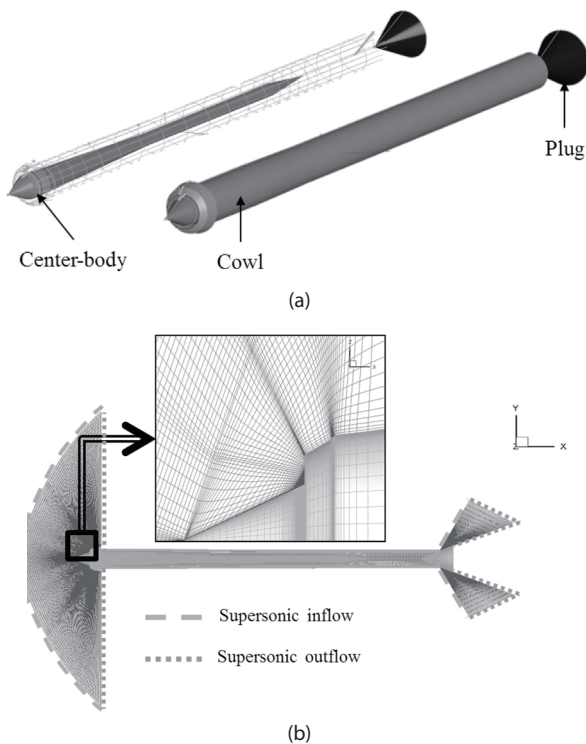


Fig. 1. Engine geometry and elements (a), grid topology and boundary conditions (b)

The plug attached at the rear part of the engine moves back and forth to control the throttling ratio (T.R). The definition of throttling ratio is explained in Fig. 2-(a).

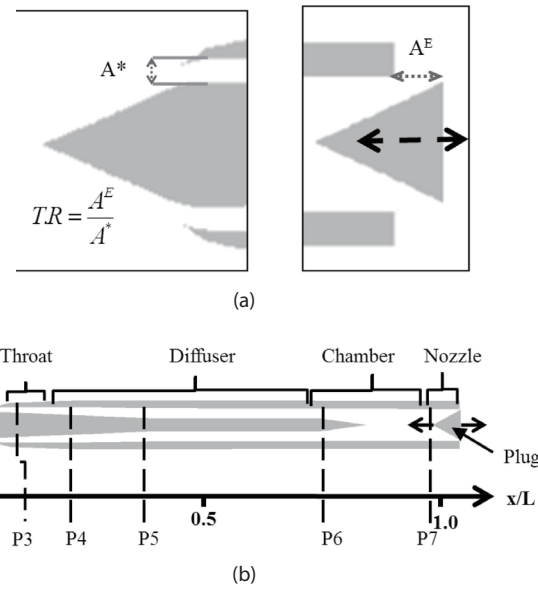


Fig. 2. Definition of throttling ratio (a) and pressure sensor locations (b)

Figure 1-(a) depicts grid topology and boundary conditions. The three-dimensional grid system consists of 80 blocks and approximately 0.7 million meshes. Half of the meshes are for the interior domain, and the dimension is 250 axial points, 35 interior radial points and 40 axis rotational points with referring to Newsome's grid [7] for turbulent flow simulation (190 of axial points 30 of interior radial points). Meshes around the compression ramp of the center body and the cowl lip section are properly clustered to obtain accurate results. The free-stream Mach number is 2 and the atmospheric condition is referred to the standard sea level air (Please clarify). The unit length is 30mm and speed of sound is 307.36m/s ($T_\infty=233k$). The computational domain is shown in Fig. 1-(b). For efficient calculations, the exterior domain is limited to two essential parts, which are near the inlet and exit. Boundary conditions for the exterior domain near the inlet are straightforward since the velocity is supersonic across the outer boundary surfaces. Mach 2 inflow conditions and simple extrapolation are applied for this part. For the other exterior domain, pressure or mass flow rate make boundary conditions easy. Without the exterior domain, pressure or mass flow rate has to be given at the exit of the chamber which might be occasionally arbitrary. Since the exterior domain includes the diverging nozzle area, flow is accelerated and velocity is supersonic across the outer surfaces of the attached domain. Thus, similar to the exterior domain near inlet, simple inflow condition (blue dashed line) and extrapolation (orange dashed line) can be applied as shown in Fig. 1-(b).

As in the experiment [6], there are seven pressure sensors

on the target geometry (Fig. 2-(b)). P1, P2 sensors are on the compression ramp and P3 is on the throat area. P4 to P7 sensors are on the diffuser and chamber surface. Pressure histories for each sensors show the inlet characteristics at each throttling ratio. Using FFT (Fast-Fourier Transform) analysis, the dominant frequency of the inlet buzz is obtained.

3. Simulation Result

The throttling ratio for the buzz simulation ranges from 0 to 0.67. With such a small throttling ratio, it is known that high frequency inlet buzz arises [6]. In general, the buzz repeats with the cycles consist of the three regimes: supercritical, critical and subcritical. For a supersonic inlet, these regimes can be clearly distinguished as shown in Fig. 3. The supersonic inlet flow conditions are defined as shown in Fig. 3.

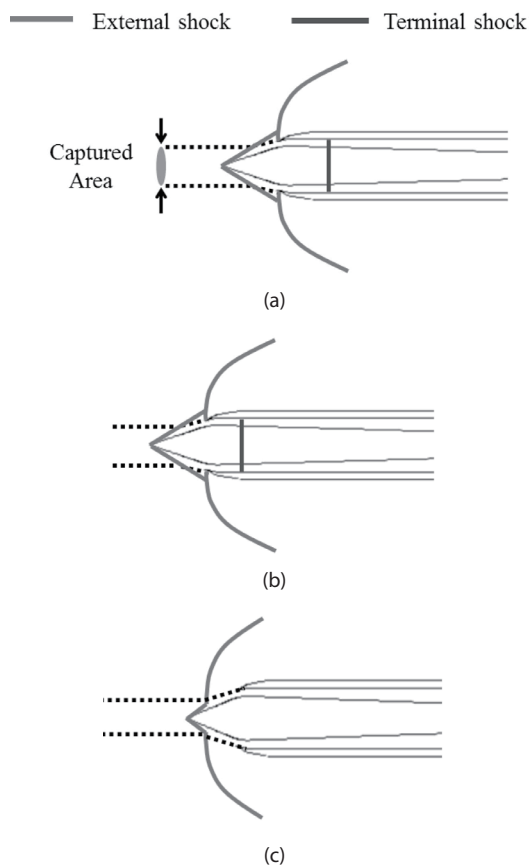


Fig. 3. Schematic images at each flow condition of supersonic inlet

3.1 Steady State Simulation at T.R 2.41

For the steady state case, both inviscid and viscous

simulations are conducted. The same numerical methods explained in the previous section are adopted to solve the three dimensional Navier-Stokes equations and the total number of mesh is increased to 3.5 million to satisfy wall resolution criteria. Internal grid dimension is 250(axial)×70(radial)×80(axis-rotational) and the turbulent non-dimensional first step size adjacent to the wall is typically $y^+=1$. In addition, $k-\omega$ SST model [17] is used to take into account the turbulence effect. Fig. 4 compares inviscid and turbulent flow simulation results for the Mach 2.0 and throttling ratio 2.41 condition. In this case, the throttling ratio is large enough to pass all of the captured air through the engine internally and thus buzz does not occur.

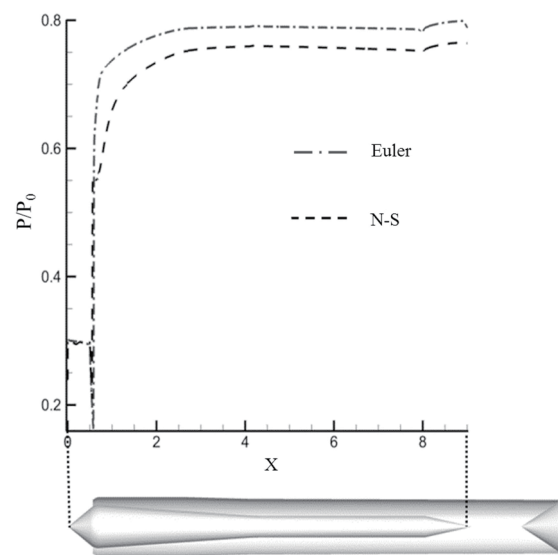


Fig. 4. Static pressure recovery curve on the center-body surface along the longitudinal direction (Mach 2.0, T.R=2.41, AOA=0°)

The curves in Fig. 4 indicate static pressure at the center-body surface along longitudinal direction. It demonstrates that different recovery behavior appears at the throat area. Afterwards, the difference is maintained to the end of the center-body. Consequently, static pressure at the plenum chamber has different quantity between inviscid and viscous simulations as listed in Table 1.

Table 1. Static pressure recovery at the plenum chamber (P_{PC} : static pressure in plenum chamber, P_0 : total pressure in settling chamber[6])

Method	Experiment[6]	Computation (N-S)	Computation(Euler)
P_{PC}/P_0	0.3	0.33	0.37

This table shows that even the viscous simulation has a difference from experimental quantity. It is because the gridded type exit of the plenum chamber in the experiment is

simplified as a continuous radial band type with maintaining an area for simulation(Please clarify). Mach number contours are shown in Fig. 5.

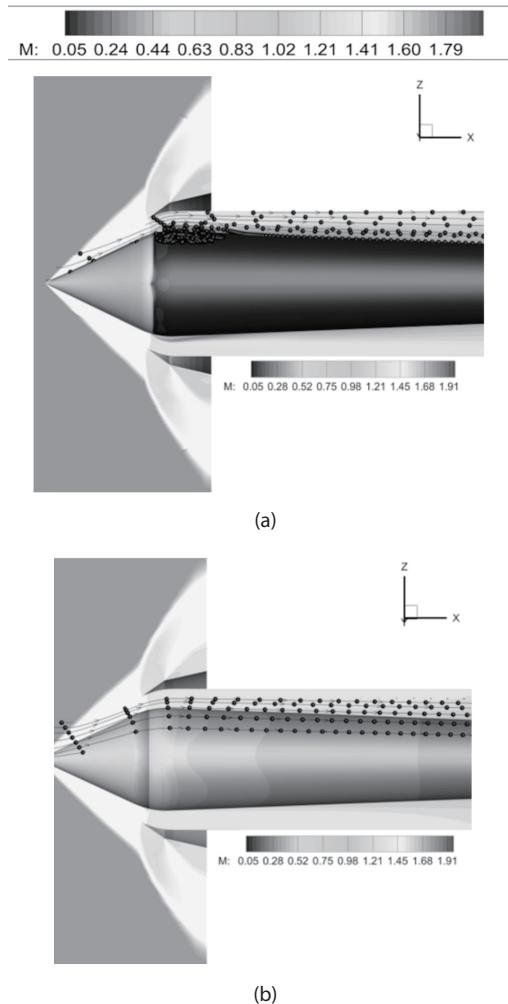


Fig. 5. Comparison of Mach number distribution around throat area(Mach 2.0, T.R=2.41, AOA=0°)

The viscous simulation result clearly shows the SWBLI induced vortex at the throat. This vortex is the main source for the pressure loss, and eventually creates a discrepancy between inviscid and viscous results. In addition, this vortex narrows the throat area and it causes throat choking earlier. The terminal shock near the cowl lip moves upstream because the throat area is decreased due to the vortex. Due to viscous effect, the viscous simulation shows the vortex near the cowl lip, 6% lower pressure recovery and lower Mach number at the wall surface in comparison with inviscid simulation, while all the simulations have the same external shock structure and common trend of pressure recovery as shown in Figs. 4 and 5.

3.2 Buzz Simulation with Zero Angle of Attack

To examine inlet buzz behavior according to the throttling ratio, the simulation was conducted with zero angle of attack. From the result of the zero throttle-area case (T.R=0), FFT analysis was carried out using pressure history data in each sensor. The dominant frequency is 334.108Hz when the physical time step of the simulation is 10 μ sec. The physical time step is controlled from 5 μ sec to 40 μ sec with growing double(Please clarify). The dominant frequencies are distributed in a span of 334.031 \pm 0.079Hz. Since it is short enough to predict a dominant frequency, 10 μ sec is adopted for the physical time step to capture instantaneous frames clearly in the high frequency buzz cycle.

Figure 6 shows shock movement and the pressure fluctuation at P₁ and P₃ sensors for the throttling ratio of zero.

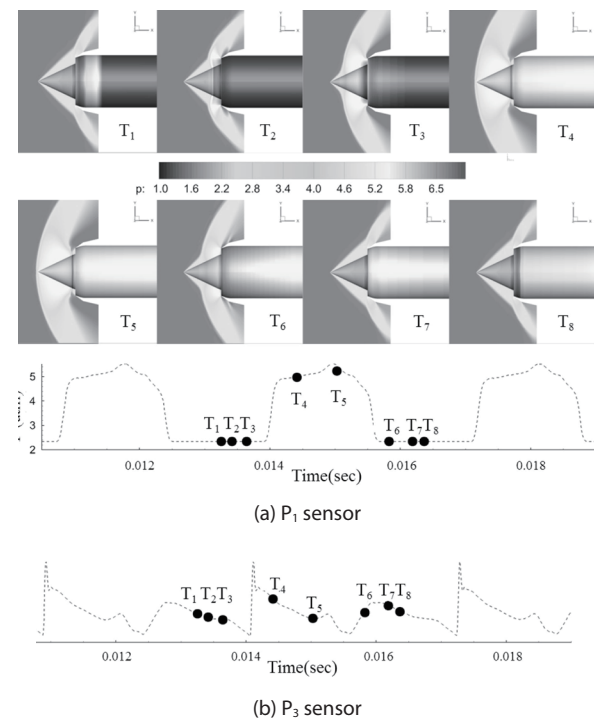


Fig. 6. Pressure oscillation sequence in the buzz cycle and pressure history at P₁ and P₃ sensors (Mach 2.0, T.R=0, AOA=0°)

The P₁ position is near the front line of the shock-expelled range, and P₃ is at the throat, which is the rear limit of terminal shock at the supercritical condition. Since the pattern of recorded pressure histories at P₁ and P₂ are almost the same, pressure data at P₁ and P₃ are presented. The frames from T₁ to T₈ are a sequence of a buzz cycle. At the beginning of the cycle, T₁, it is a supercritical condition and internal pressure is increasing due to blocked exit (T.R is 0). Therefore, the high pressure region is expanded to upstream-wise, and by the time it reaches the cowl lip, the flow regime

suddenly switches from a supercritical to a subcritical condition, as shown in Fig. 6, T_2 . During the time interval of T_3 to T_4 , the shock passes the sensor position with a step-like pressure jump. The shock moves so fast that the flow regime instantly switches from a supercritical to a subcritical state. In the subcritical condition, the back-pressure wave is still moving to upstream-wise and the oblique shock and the bow shock interact with each other. After all, the bow shock is detached from the tip of the center-body cone. During this shock forwarding process, from T_1 to T_4 , the captured ratio is decreased and high back-pressure is relieved with emission by reversed flow. The next stages from T_5 to T_8 are the shock retreat process. The captured area increases as the shock moves downstream and the flow regime returns to the supercritical condition. From T_8 , after a while, the internal pressure rises and the flow structure becomes that in T_1 again. Therefore, one buzz cycle is over and it repeats. This sequence of the buzz cycle has been well known by many studies and the buzz behavior of this simulation result agrees well with the previous researches [4-9].

Figure 7 depicts the dominant frequency variation with different throttling ratios. The variation is compared to the experiment and turbulent flow simulation results [13].

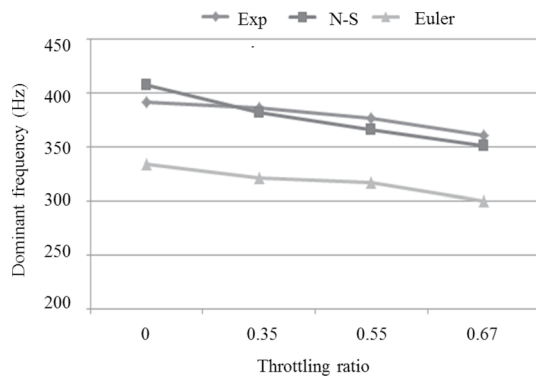


Fig. 7. Dominant frequency variation along the throttling ratio

Current inviscid results predict a lower frequency than the viscous simulation, but the gap between the two curves is nearly constant as 60Hz or 15% and the tendency of frequency variations also coincide. As mentioned in section 3.1, since there are no boundary layers and a separation vortex in the inviscid simulation, the throat is choked later than the viscous case. Therefore, the inlet captures more mass flow so that beginning of the shock forwarding process is delayed and the buzz cycle takes longer time.

The comparison studies between inviscid and turbulent flow simulations show that although there are some quantitative differences, inviscid flow calculation predicts the external shock structure and the tendency of buzz

frequency well. In the meantime, the turbulent flow simulation takes approximately 10 to 20 times more computational cost than the inviscid one. Thus, in the next step, we decided to perform inviscid flow calculations to study the qualitative flow behavior around the inlet. In fact, it was found that the inviscid calculation was sufficient to examine the asymmetric unstable behavior of buzz flow with a non-zero angle of attack.

3.3 Buzz Simulation with Moderate Angle of Attack

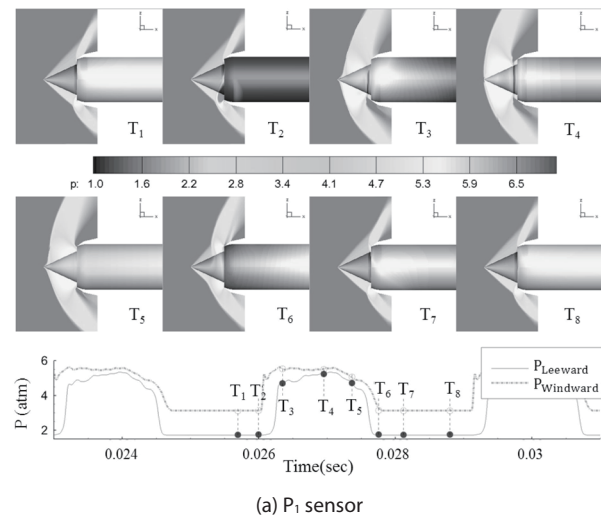
In this section, the effects of different attack angles are studied on the buzz phenomenon. The attack angles of 3° , 5° , 7° and 10° are chosen. Table 2 lists the dominant frequencies varying with different angles of attack. Although the attack angle increases, the frequency is nearly stationary at around 334Hz, thus the buzz frequency is also not that sensitive to the attack angle.

Table 2. Dominant frequency variation along the angle of attack at a throttling ratio of 0

		AOA				
		0°	3°	5°	7°	10°
T.R = 0	Frequency (Hz)	334.108	336.242	334.975	334.089	334.625

This tendency has already been reported by precedent experimental studies [6, 11, 12].

Figure 8 shows the sequence frames in a buzz cycle at a 10° angle of attack and 0 throttling ratio. The sequence is similar to Fig. 6 while the asymmetric shock structure is observed.



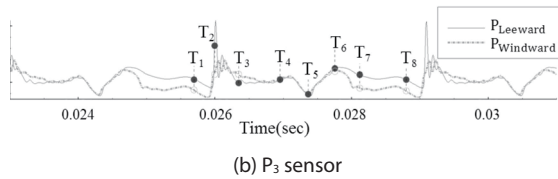


Fig. 8. Pressure oscillation sequence in the buzz cycle and pressure history at P_1 and P_3 sensors of wind/leeward side (Mach 2.0, $T.R=0$, $AOA=10^\circ$)

Since the oblique shock strength at the windward side (lower half) is stronger than the leeward side (upper half), pressure at windward rises greater than the other side. It is supported by pressure history curves at the bottom of Fig. 8, which are measured at the P_1 and P_3 position. In the shock forwarding process (T_1 to T_4), shock in the leeward side moves out later than the shock in the other side. Using the Taylor-Maccoll [18] equation, asymmetric oblique shock angles can be predicted. However, the asymmetric bow-shock structure in the T_4 frame of Fig. 8 and desynchronized shock oscillation need to be explained further.

Figure 9 presents the Mach contours and stream lines at a critical condition when there is no angle of attack (T_7 frame in Fig. 6) when the throttling ratio is 0, which is T_7 , one of the frames in Fig. 6.

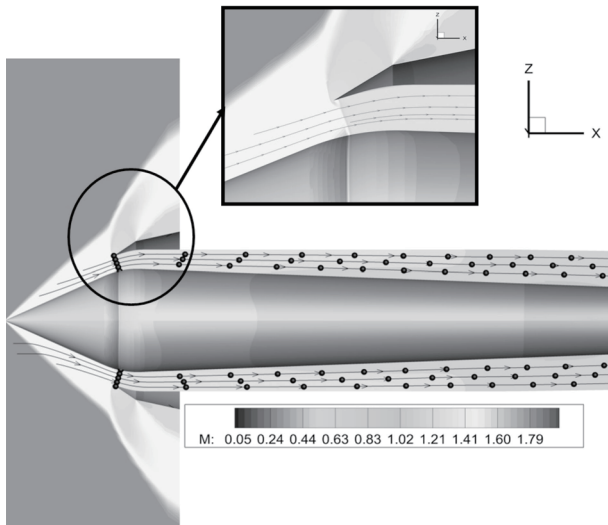


Fig. 9. Mach contour and stream line at the T_7 frame in Fig. 6 (Mach 2.0, $T.R=0$, $AOA=0^\circ$)

The normal shock remains at cowl lip in both the windward and leeward side. On the other hand, Fig. 10 shows the asymmetric shock structure. This is from the T_7 time frame in Fig. 8.

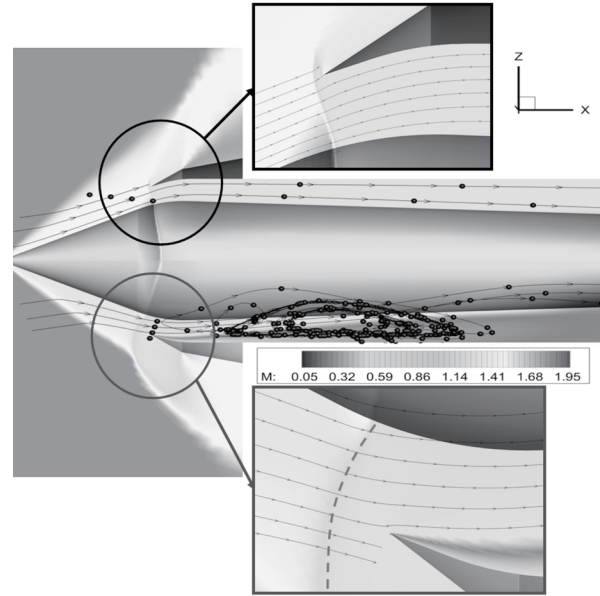


Fig. 10. Mach contour and stream line at the T_7 frame in Fig. 9 (Mach 2.0, $T.R=0$, $AOA=10^\circ$)

Furthermore, bow shock (dashed line in Fig. 10) occurs at the windward side and a slip line is generated from the cowl lip. Due to the windward bow shock, the direction of the flow stream is changed not to align with the inner cowl surface. By the reason (Ed. note: This is confusing. Do you mean, 'By this reason?' or 'For this reason'? Please review and clarify), there is a large amount of velocity difference between the mainstream and the flow near the inner cowl surface. However, there is very little pressure gradient across this slip line. This slip line is one of the sources of distortion and one experiment reported that flow separation occurred at the windward cowl lip [21]. During the shock retreat process from T_5 to T_8 , pressure on the leeward side is higher than the windward side at P_3 . This is because the pressure discontinuity surface leans upstream-wise at the leeward side as depicted in Fig. 8-(a) T_6 , T_7 frames. This shock-leaning behavior becomes more visible as the throttling ratio increases (see Fig. 12-(a) T_6 , T_7).

Generally, in attack angled flow field, the effective angle of incidence increases at the windward compression side whereas it decreases at the other side. Therefore, the leeward oblique shock strength is weaker than the no attack angled case and pressure less rises (Please clarify) after the oblique shock. In Fig. 10, since back pressure is relatively much higher than the pressure after the oblique shock at the leeward side, the shock is eventually pushed out of the inlet. A few time frames for the non-zero angle of attack case are depicted schematically in Fig. 11.

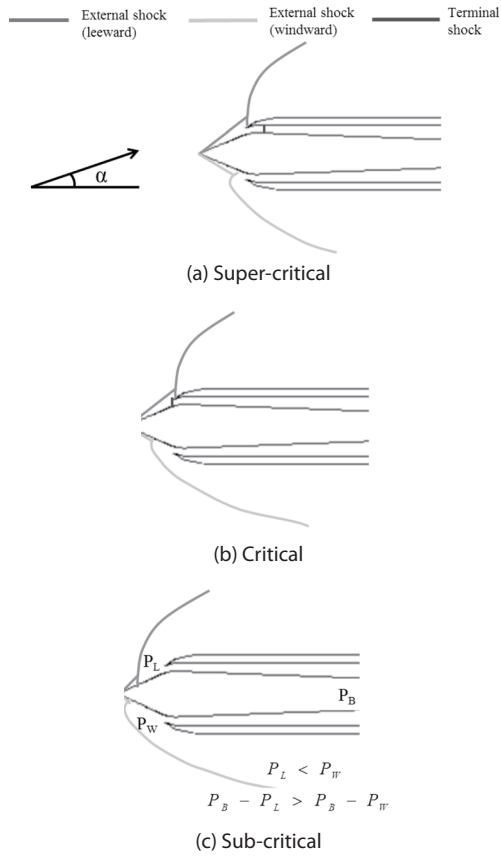


Fig. 11. Schema of asymmetric flow regime at the angle of attack (P_L : leeward aftershock pressure, P_W : windward aftershock pressure, P_B : back pressure)

Figure 10 frame (T_7) is simplified in Fig. 11-(b). At this moment, leeward terminal shock moves to a more upstream position than the zero angle of attack case (Fig. 9) due to weaker leeward oblique shock. Meanwhile in the windward side, stronger oblique shock was expected to create the supercritical condition with the terminal shock residing inside. However, a bow shock is generated in front of the cowl lip due to the increased bluntness of the windward cowl lip. Therefore, the windward side is also in subcritical condition and the slip line is developed in the cowl lip because the bow shock makes the windward inflow direction curved as shown in Fig. 10. Figure 11-(c) shows when the shock is pushed out to the upstream limit in Fig. 8 T_4 . The shock angle depends on three conditions: free-stream Mach number, compression surface angle, and back pressure. As shown in Fig. 11-(c), after-shock pressure on the leeward side is lower than the windward side even if back pressure is equal and high on both sides. As a result, back pressure on the leeward side expels the leeward shock more strongly, and thus the leeward bow shock angle is larger than the windward side in the subcritical condition. During the process of Figs. 11-

(a) to (c), the inlet captured area keeps being asymmetric and varies in a buzz cycle. As a result, this transient behavior makes the dynamic distortion of the total pressure at the inlet cross section.

When the throttling ratio is increased, shock movement at the windward and leeward side is even more desynchronized with each other compared to the zero throttle-area case. As shown in Fig. 12, during shock forwarding ($T_1 \sim T_4$), process shock positions at the windward and leeward side have more different features than the previous case (Fig. 8). Also, Fig. 12 shows that windward pressure at the P_1 sensor increases before T_2 , which is earlier than the zero throttle-area case.

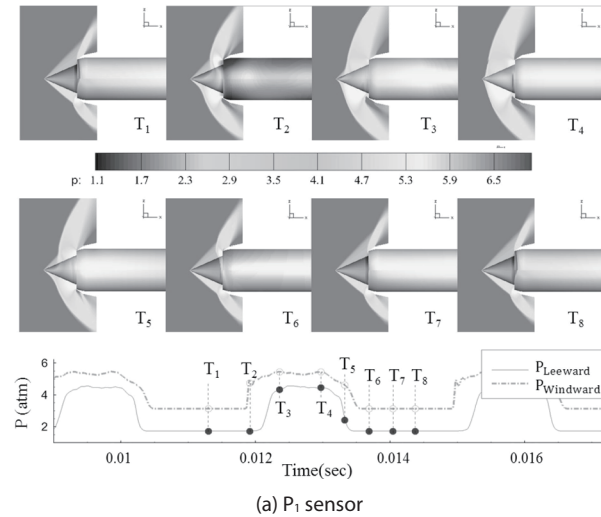


Fig. 12. Pressure oscillation sequence in the buzz cycle and pressure history at P_1 and P_3 sensors of wind/leeward side (Mach 2.0, $T.R=0.35$, $AOA=10^\circ$)

As mentioned earlier, a bow shock is located in front of the windward cowl and there is always some open space between the shock and the cowl lip. Therefore, it is easier to push flow upstream and reversing flow has room to escape. It makes the windward shock move upstream earlier. The leeward side, on the other hand, requires higher back pressure for a transition to subcritical because the shock at the cowl lip should be pushed away first. Only then, can the flow be emitted out of the inlet. Since pressure rises slower as the throttling ratio increases, the leeward side shows slower transition to the subcritical state, which results in even more severe desynchronizing with the other side.

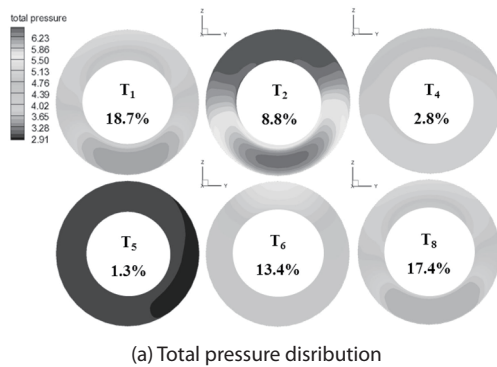
3.4. Distortion at Inlet Cross Section Induced by Asymmetric Physics

In general, a ramjet with an angle of attack has an internal distortion problem in which pressure distribution as well as reaction amount are significantly irregular. This irregularity becomes severe as angle of attack increases. In particular, the inlet buzz with an angle of attack incurs dynamic distortion. The distortion coefficient (DC) is defined as follow [19]:

$$DC = \frac{\max P_t - \min P_t}{\bar{P}_t}, \quad (2)$$

(\bar{P}_t : averaged total pressure, P_t : maxim or minimum total pressure at the cross section)

Time indices in Fig. 13 are from Fig. 8, and DC is written in percent unit in the figure.



(b) Distortion history at P₄

Fig. 13. Total pressure distribution and distortion history at P₄ (Mach 2.0, T.R=0, AOA=10°)

DC is higher during the back pressure recovery stage (T_1 , T_2 , T_6 , and T_8). During these times the terminal shock remains near the cowl lip and the throat section is exposed to a high Mach number and low pressure flow. Asymmetric resources such as slip line from the windward cowl lip in Fig. 10 and reversed flow desynchronizing strongly affect distortion. Figure 14-(a) shows the time averaged distortion coefficient for different throttling ratios. It appears that the throttling ratio does not affect the distortion much. However, the angle of attack is found to significantly influence the distortion. As is shown in Fig. 14-(b), DC increases nearly in proportional to the attack angle. Although the averaged distortion coefficient is less than 0.1 but instantaneous peak is more than 0.2, 3 to 7 times higher than the averaged

DC.(Ed. note: This is confusing. Please clarify)

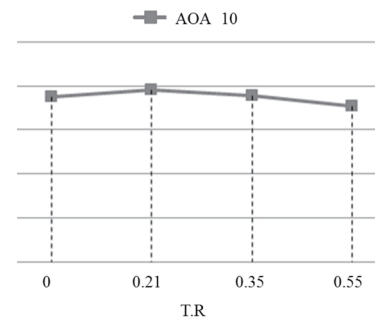
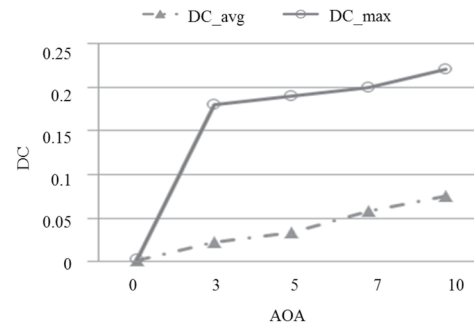


Fig. 14. Averaged and maximum distortion coefficient variation along the attack angle (left, Mach 2.0, T.R=0) and averaged distortion along the throttling ratio (right, Mach 2.0, AOA=10°)

4. Conclusion

The inlet buzz was numerically simulated with controlling the throttling ratio from 0 to 0.67 and the angle of attack from 0° to 10°. When there is no angle of attack, the inviscid simulation predicted a dominant frequency 15% lower than the viscous simulation and experimental result but the slope of the dominant frequency variation for different throttling ratios agrees well with each other. The asymmetric shock structure and flow physics appear when the angle of attack exists. Due to weaker shock strength, back pressure pushes leeward terminal shock to a more upstream location. In the windward side, a bow shock appears in front of the windward cowl due to the increased bluntness of the cowl lip. Since the stream line is curved by the bow shock, a slip line is generated from the windward cowl lip. Further, the moment of reversed emission at windward and leeward is desynchronized as the throttle ratio increases. These asymmetric physics at the angle of attack condition dominantly affect distortion. For this reason, angle of attack is the determinant in regards to distortion while the throttling ratio is a minor element. In this study, inviscid computations are conducted to reduce

computational resources and time cost. Although the present result shows some quantitative difference from the experimental data, it reasonably predicts the effect of angle of attack on the buzz frequency, shock structure and distortion coefficient. This information allows us to understand the fundamental aerodynamic characteristics, such as buzz behavior and inlet performance, of target geometry within a limited range of angle of attack. Moreover, the computed results can be used for preliminary design and identifying a feasible range of inlet operations.

Acknowledgement

This work was supported by the KISTI Supercomputing Center (KSC-2010-C1-0031), the National Research Foundation of Korea (NRF) grant funded by the Korea government(MEST) (No. 2011-0027486) and NSL (National Space Lab.) program through the National Research Foundation of Korea funded by the Ministry of Education, Science and Technology (Grant 2011-0029871).

References

- [1] Connors, J.F., "Some Aspects of Supersonic Inlet Stability", NACA RM-E55L16a, 1956.
- [2] Kwak, J.Y., Hong, W., Shin, S. J., Lee, I., Yim, J. W., and Kim, C., "Static Aeroelastic Analysis of a Supersonic Flight Vehicle with a Ramjet Engine", *51th AIAA/ASME/AHS/ASC Structures, Structural Dynamics, and Materials Conference*, Orlando, Florida, April 2010.
- [3] Oswatitsch, K., "Pressure Recovery in Missiles with Reaction Propulsion at High Supersonic Speeds (the Efficiency of Shock Diffusers)", NACA TM-1140, 1947.
- [4] Dailey, C.L., "Supersonic Diffuser Instability", *Journal of the Aeronautical Sciences*, Vol. 22, No. 11, 1955, pp. 733-749.
- [5] Ferri, A., and Nucci, R. M., "The Origin of Aerodynamic Instability of Supersonic Inlets at Subcritical Conditions", NACA RM-L50K30, 1951.
- [6] Nagashima, T., Obokata, T., and Asanuma, T., "Experimental of Supersonic Air Intake Buzz", Institute of Space and Aeronautical Science of Tokyo, JAPAN, Rept. 481, May 1972.
- [7] Newsome, R. W., "Numerical Simulation of Near-Critical and Unsteady, Subcritical Inlet Flow", *AIAA Journal*, Vol. 22, No. 10, 1984, pp. 1375-1379.
- [8] Lu, P., and Jain, L., "Numerical Investigation of Inlet Buzz Flow", *Journal of Propulsion and Power*, Vol. 14, No. 1, 1998, pp. 90-100.
- [9] Trapier, S., Deck, S., and Duveau, P., "Detached-Eddy Simulation and Analysis of Supersonic Inlet Buzz", *AIAA Journal*, Vol. 46, No. 1, 2008, pp. 118-131.
- [10] Bendot, J.G., Heins Jr., A.E., and Piercy, T.G., "Ramjet Air Induction System Design for Tactical Application", Ramjet and Ramrocket Propulsion System for Missiles, AGARD Lecture Series No.136, 1984.
- [11] Lee, H.J. and Jeung, I.S., "Experimental and Numerical Investigation on the Supersonic Inlet Buzz with Angle of Attack", *Shock Waves*, Part XVI, 2009, pp. 1111-1116.
DOI: 10.1007/978-3-540-85181-3_51
- [12] Soltani, M.R., Farahani, M. and Asgri Kaji, M.H., "An Experimental Study of Buzz Instability in an Axisymmetric Supersonic Inlet", *Scientia Iranica B*, Vol. 18, No. 2, 2011, pp. 241-249.
- [13] Hong, W. and Kim, C., "Numerical Study on Supersonic Inlet Buzz under Various Throttling Condition and Fluid-Structure Interaction", *29th AIAA applied Aerodynamics Conference*, Honolulu, Hawaii, June 2011.
- [14] Kim, K. H., Kim, C., and Rho, O. H., "Methods for the Accurate Computations of Hypersonic Flows, Part 1: AUSMPW+ Scheme", *Journal of Computational Physics*, Vol. 174, No. 1, 2001, pp. 38-80.
- [15] Van Leer, B., "Towards the Ultimate Conservative Difference Scheme. V. A Second Order Sequel to Godunov's Methods", *Journal of Computational Physics*, Vol. 32, No.1, 1979, pp. 101-136
- [16] Yoon, S., and Jameson, A., "Lowe-Upper Symmetric-Gauss-Seidel Method for the Euler and Navier-Stokes Equations", *AIAA Journal*, Vol. 26, No. 9, 1988, pp. 1025-1026.
- [17] Menter, F. R., "Two-Equation Eddy-Viscosity Turbulence Model for Engineering Applications", *AIAA Journal*, Vol. 32, No. 8, 1994, pp. 1598-1605.
- [18] Kopal, Z., "Tables of Supersonic Flow around Cones of Large Yaw", Massachusetts Institute of Technology, Technical report No.5, 1949.
- [19] Schueller, C.F. and Stitt, L.E., "An Inlet Design Concept to Reduce Flow Distortion at Angle of Attack", NACA RM-E56K28b, 1957.
- [20] Seddon, J., and Goldsmith, E.L., *Intake Aerodynamics*, AIAA Education Series, 1999.
- [20] Goldsmith, E.L., "Some Aspects of Engine and Airframe Integration for Ramjet and Ramrocket powered Missiles", Ramjet and Ramrocket Propulsion System for Missiles, AGARD Lecture Series No.136, 1984.